Published in : ACS Sustainable Chemistry & Engineering (2020), vol. 8, issue 15, pp. 5868-5879
DOI: 10.1021/acssuschemeng.9b07434
Status : Postprint (Author's version)

RECOVERY OF NANO-STRUCTURED SILICON FROM END-OF-LIFE PHOTOVOLTAIC WAFERS WITH VALUE-ADDED APPLICATIONS IN LITHIUM-ION BATTERY

Nicolas Eshraghi[1], Loris Berardo[1], Audrey Schrijnemakers[1], Vincent Delaval[1], Mahdokht Shaibani[2], Mainak Majumder[2,a], Rudi Cloots[1], Bénédicte Vertruyen[1], Frédéric Boschini[1], and Abdelfattah Mahmoud[1,b,*]

1. GREENMAT, CESAM Research Unit, Department of Chemistry, University of Liege, 4000 Liege, Belgium
2. Nanoscale Science and Engineering Laboratory (NSEL), Department of Mechanical and Aerospace Engineering, Monash University, Clayton, Victoria 3168, Australia
a orcid.org/0000-0002-0194-9387
b orcid.org/0000-0002-4899-859X
** Corresponding Author*

Abstract:

Millions of residential and industrial solar panels installed in the late 1980s and early 1990s are approaching the end of their life, resulting in the drastic accumulation of a potential source of environmental pollution—given the presence of hazardous materials, such as lead. The foreseen crisis, however, can be turned into a great opportunity by value-added recovery of precious solar-grade silicon (Si) to the highly desired nanostructured silicon for lithium-ion batteries (LIBs). Herein, we demonstrate a potential end-of-life management option for photovoltaic (PV) panels, representing a step toward producing greener and more energy-efficient Si for batteries. We show that leaching the recovered silicon wafers in critically tuned alkali-acid leaching baths effectively removes the major impurities: lead (Pb), silver (Ag), and aluminum (Al). The ultrapure Si is then nanosized via industrially scalable milling routes to meet the requirements of expansion-tolerant Si anodes for LIBs delivering capacities as high as 1400 mAh g^{-1}.

Keywords: Photovoltaic panel, Recovery, Sustainable, Recycling, Silicon anode, Ball milling

Introduction

The domestic and industrial uptake of solar power has significantly contributed to producing renewable and clean energy for approximately 25 years now. To close the loop in the energy cycle, the next mission of the solar panel industry is the recycling of end-of-life photovoltaic panels (PV). The substantial PV installations occurred in the late 1980s and early 1990s, followed by dramatic growth in early 2000s. With an average lifespan of up to 25−30 years for the solar panels, the world is set to face another recycling crisis, urging governments to develop end-of-life schemes for PV panel waste.[1,2]

As of mid-2012, the recast WEEE (Waste Electrical and Electronic Equipment) Directive 2012/19/EU mandates European countries to adopt PV waste management programs in which producers are responsible for the take-back and recycling of the panels they sell. The goal of these policies is to develop greener products and make recycling more affordable and economically sustainable by leading producers

Published in : ACS Sustainable Chemistry & Engineering (2020), vol. 8, issue 15, pp. 5868-5879
DOI: 10.1021/acssuschemeng.9b07434
Status : Postprint (Author's version)

to factor in the cost of the collection and end-of-life treatment of their products into the cost paid by the consumers.[3]

Silicon-based photovoltaic modules are predominantly made of glass, aluminum (Al), polymers, and silicon (Si), as well as metallic contacts such as silver (Ag) or potentially hazardous materials such as lead (Pb).[4] The presence of precious materials such as copper (Cu), Ag, and particularly solar grade Si, however, could turn this potential recycling crisis into an opportunity.[5−11] If done right, there could be significant energy savings by recovering silicon from the modules, as solargrade silicon is extremely energy-intensive due to its ultrahigh purity. It is noteworthy that the most energy-intensive step in the production of silicon modules is the Siemens process, which converts $SiHCl_3$ to ultrapure silicon. If the silicon recovered from the modules meets the specifications of solar-grade silicon, it will advantageously bypass the Siemens process. Considering the high quality, the recovered Si could find applications in avenues where high purity is key; for example, it can be used as new feedstock for the PV industry or as the active material in the negative electrode of the 3b generation of lithium-ion batteries (LIBs).

High capacity electrode materials could bring major performance breakthroughs to today's LIBs. One such an example is the use of Si as a replacement for low capacity graphite, in the so-called Generation 3b of LIBs. Silicon, with its ultrahigh capacity of 4200 mAh g^{-1}, offers tremendous potential, however, the capacity is so large that the cycling stress makes the electrode fall apart after less than 10 cycles. To this end, tremendous effort has been made to enhance the performance of silicon anodes in LIBs and particularly to overcome and accommodate the volume expansion issue during the charge/discharge processes. The research approaches could be classified into three classes: (i) the formation of silicon composites; (ii) the structuration of silicon composite, hollow, yolk−shell, pomegranate, etc. structures;[19−23] and (iii) the nanostructuration of silicon particles, in order to form materials with tailored one-, two-, or three-dimensional structures.[24−28]

Herein, we introduce an all-around platform for the value-added recovery of high purity Si and its simple nanostructuration for direct application as a high-performance anode material in LIB. We demonstrate that a critically controlled yet industrially adaptable leaching process enables the effective removal of Pb, Al, and Ag, leaving behind ultrapure nanometric to micrometric silicon particles. Nanosizing of the Si particles was done by a carefully optimized milling process—certainly an inexpensive route compared to chemical vapor deposition (CVD) and or structuration from nanopowder precursors.[29,30] We show that the high purity of Si recovered from PV panels along with its nanostructuration as a result of milling results in delivery of capacities as high as 1400 mAh g^{-1} when used as an anode material in LIBs, promising for a greener quality, inexpensive electrode material.

Experimental section

Leaching of the Solar Cells.

The leaching treatment is performed on polycrystalline silicon wafer scraps from photovoltaic cells. The wafer scraps used here were either broken wafer scraps from fabrication or were obtained from photovoltaic modules (provided by RECMA as part of the SOLARCYCLE project) after a hydrothermal treatment under a subcritical atmosphere previously reported by Schrijnemakers et al. to separate the component.[4] In a typical experiment, a sample composed of a few centimeter-sized wafer fragments is

Published in : ACS Sustainable Chemistry & Engineering (2020), vol. 8, issue 15, pp. 5868-5879
DOI: 10.1021/acssuschemeng.9b07434
Status : Postprint (Author's version)

inserted successively into two distinct alkali-acid leaching baths under vigorous stirring. A combination of potential leaching solutions was studied by varying the concentration and temperature of the leaching solution and the total leaching time as shown in Tables S1 and S2. In the optimized leaching process, the alkali leaching bath consists of 8 mol/L potassium hydroxide (KOH) solution heated at 60 °C for 5 min. This first step aims to remove the Al layer on the bottom side of the silicon wafer, which is a principal source of impurities. The second bath targets the leaching of the screen-printed layer on the top side, composed of Ag and Pb. This reaction is performed using an 8 mol/L nitric acid (HNO_3) solution heated at 80 °C for 15 min. Upon successful leaching treatments, the wafer fragments are washed with deionized water to remove traces of bath solutions as well as dissolved Al, Pb, and Ag and followed by drying in an oven at 120 °C.

Ball Milling of Extracted Silicon from Photovoltaic Cells.

Nanosizing of the Si particles is key in achieving good cycle life when used as an electrode material in LIBs. To study the electrochemical performance of extracted silicon from PV cells, first the centimeter sized wafer scraps were converted into fine powders (<125 μm) in the pregrinding step. Next, 800 mL (435g) of silicon wafer fragments along with alumina balls (5.8 kg of Ø25 mm and 2 kg of Ø10 mm) are introduced into the grinding chamber (5 L capacity) of a stainless-steel tumbling ball mill device operated at 75% of the critical speed (cataract mode). With low rotational speed, a gentle tumbling action is observed in the balls, but as the speed increases the tumbling action converts to a cascading state. Further increasing the rotational speeds (70−80% of critical speed) forms a cataract of balls, which will improve the size reduction efficiency.

In the next step for nanosizing of the Si particles, an inert atmosphere is needed to prevent the oxidation of Si particles during the milling as the surface area increases. The sample composed of 6 g of the pregrinded powder and tungsten carbide balls (8 mm diameter) was charged into a 50 mL tungsten carbide grinding jar within an argon-filled glovebox. The powders were mechanically milled with a planetary ball mill. First, the milling was carried out at various milling speeds (100 to 400 rpm) during 20 h to investigate the optimum energy needs (varied by modifying the milling speed) to break down Si particles. Upon identifying the optimum milling speed (250 rpm), the silicon powder was milled for various periods (1 to 40 h) to identify the minimum time needed to obtain a high-performance Si anode.

Characterizations.

X-ray diffraction (XRD) was carried out to identify the obtained phases over the 2θ range from 25° to 90° with a Bruker D8 Twin−Twin powder diffractometer using Cu Kα radiation. The morphology of Si wafers and ball-milled silicon were studied using a scanning electron microscope (XL 30 FEG-ESEM, FEI). The composition of Si wafers was checked using Energy-Dispersive X-ray Spectroscopy (EDS) analysis and inductively coupled plasma mass spectrometry (ICP-MS) to monitor the efficiency of the leaching process. Particle-size distribution was determined using a Mastersizer 2000 particle size analyzer. BET surface area measurements were carried out to analyze any changes in specific surface area with milling speed and duration. This was done using BET nitrogen gas adsorption with the Micromeritics ASAP 2020 Plus. Samples were degassed at 150 °C for a total of 12 h prior to analysis.

Electrochemical measurements were conducted in two-electrode coin cells, using high purity lithium metal foil (Chemetall, Foote Corp USA) as counter electrode material which also operated as the reference electrode and 1 M $LiPF_6$ in ethylene carbonate/dimethyl carbonate (EC:DMC 1/1, v/v) with 10 wt % FEC and 2 wt % VC as the electrolyte. Silicon active material was mixed with carbon black (CB) and carboxymethyl

Published in : ACS Sustainable Chemistry & Engineering (2020), vol. 8, issue 15, pp. 5868-5879
DOI: 10.1021/acssuschemeng.9b07434
Status : Postprint (Author's version)

cellulose (CMC) in 1:1:1 ratio and then mixed in water for 2 h and spread on a Cu foil substrate. The electrodes were dried for 12 h at 110 °C under a vacuum to remove the water. The electrodes were then cut into disks 12.6 mm in diameter (active mass of approximately 1−2 mg). The current collectors were stainless steel, and the separator between electrodes was a 25 μm monolayer polypropylene membrane (Celgard 2500). All the assembly processes for the coin cells were conducted in an argon-filled glovebox. All cells were tested within a fixed voltage window, between 0.01 and 1.0 V vs Li^+/Li^0 in galvanostatic mode (1C corresponds to the current for x = 1 in Li_xSi in 1 h), using the BTS4000 Neware Electrochemical Test System. All electrochemical tests were carried out at room temperature.

Results and discussion

Leaching of Si Wafers.

The silicon wafer (photovoltaic cell) fragments were analyzed before and after the alkali-acid leaching treatment as described in the Experimental Section to draw a comparison between unleached, KOH-leached, and KOH/HNO_3-leached wafers. To bring the innovative processing into context, we note that a large number of approaches to recycle Si from PV wastes have used variants of Wright etch and Buffered Oxide Etch (BOE), which contained hydrofluoric acid (HF), to remove the antireflection coating, p−n junction, and the metal-containing connections present in PV panels (Table S3).[31−36] A major limitation for industrial application of HF is that it is of a hazardous nature (highly corrosive and toxic for users and environment) and has added costs in the process, thus we avoid using it in our work.[37] HF-free approaches use either sulfuric acid or phosphoric acid leaching or an additional mechanical removal step to remove the antireflective coating as presented in Table S3.

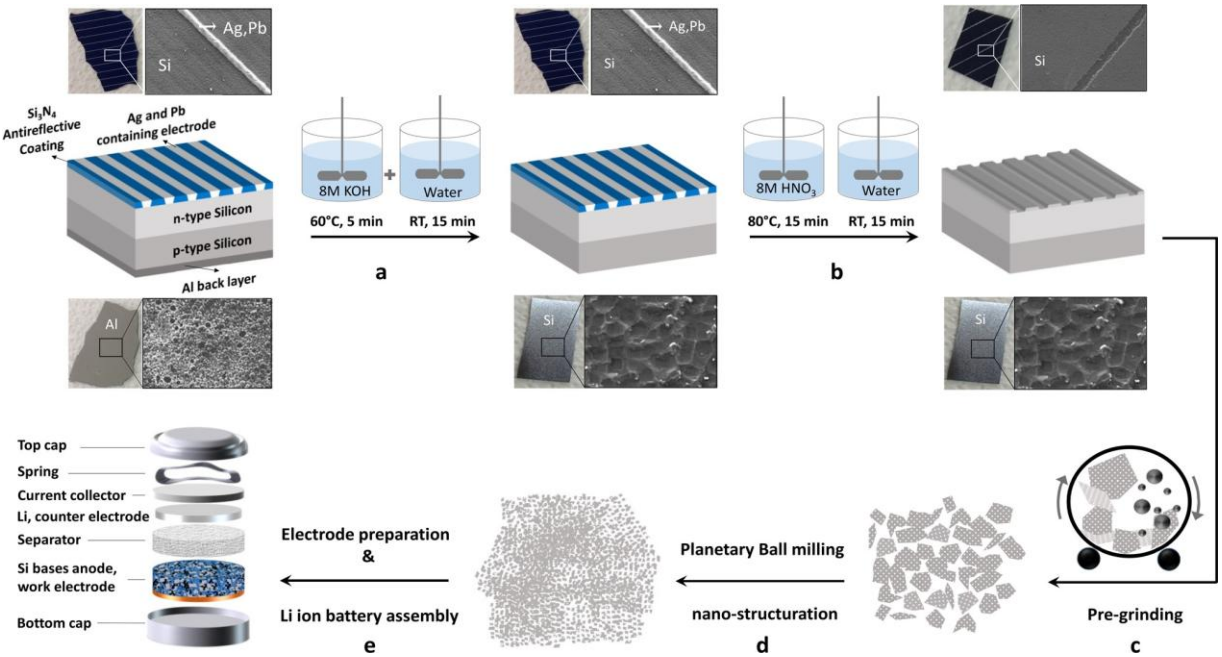

Figure 1. Schematic illustration of the sustainable recovery of Si from PV panels for application in LIBs: After dismantling the PV panel, (a) controlled leaching process using KOH will enable the effective removal of Al from the bottom side of the wafer followed by washing the fragments to remove traces of KOH. (b) The Ag−Pb channels and the thin Si_3N_4 layer on the top side of the wafer are removed using HNO_3 solution. HNO_3 is highly oxidizing so in case this step is done prior to the KOH treatment, a passivation layer of aluminum oxide will be formed on the back layer. (c) The intact or centimeter sized Si wafer scraps were transformed into a coarse powder using a rolling ball mill in the pregrinding step. (d) Further downsizing the powder using a planetary ball mill to obtain fine silicon powder that will be used as anode material for Li-ion batteries. (e) Si based anode preparation was done by adding a dry mixture of silicon powder, carbon black, and CMC in a 1:1:1 ratio to a pH 3 buffer solution and coated on copper foil. The dried electrode is then assembled in coin cell configuration for further tests.

Published in : ACS Sustainable Chemistry & Engineering (2020), vol. 8, issue 15, pp. 5868-5879
DOI: 10.1021/acssuschemeng.9b07434
Status : Postprint (Author's version)

The advantage of our dual-bath leaching is the highly efficient and selective removal of Al, Ag, and Pb without oxidizing the Si layer. Our approach allows for high removal efficiency by leaching as high as 400−500 g of wafers scraps using 1 L of 8 M KOH at 60 °C and up to 800 g of wafer scraps using 1 L of 8 M HNO_3 at 80 °C.

SEM micrographs presented in Figure 1 show the morphology of unleached and leached silicon wafer fragments. The back/bottom side of the silicon wafer is uniformly covered with spherical Al/Al oxide particles, and on the front/top side, a series of Ag/Pb channels are present to ensure the electrical conduction in the silicon wafer surface.

After the leaching process, silicon wafer fragments show very different morphological features. Polycrystalline silicon is clearly visible on the back/bottom side in the SEM images indicating that the Al layer was removed from the surface (Figure S1). Al reacts with KOH to produce hydrogen because the excess hydroxide ion (OH^-) first attacks the tough Al_2O_3 layer so the metal can react more efficiently.[38] Aluminum converts to the tetrahydroxoaluminate ion $Al(OH)_4^-$, and the reaction is considered a dissolution (eq 1). On the front side, the Ag/Pb has been leached by HNO_3 solution treatment, and the silicon is visible at the bottom of the trenches. Leaching of the two electrodes is explained by the following reactions (eqs 1−4):

Al leaching: $2Al + 2KOH + 6H_2O \rightarrow 2K^+ + 2Al(OH)^-_4 + 3H_2\uparrow$ (1)

Ag leaching: $Ag + 2HNO_3 \rightarrow AgNO_3 + H_2O + NO_2\uparrow$ (2)

Pb leaching: $Pb + 2HNO_3 \rightarrow PbO + H_2O + 2NO_2\uparrow$ (3)

$PbO + 2HNO_3 \rightarrow Pb(NO_3)_2 + H_2O$ (4)

It is imperative that due to the highly oxidizing nature of nitric acid, the removal of Al by the KOH solution treatment must be done first to avoid the formation of a passivation layer of aluminum oxide.

To examine the efficiency of the leaching process and determine the purity of the resulting silicon, both unleached and leached cell fragments were analyzed by ICP-MS. The concentrations (in wt %) of elements in the feedstock (unleached silicon wafer) and after each leaching step are collected in Table 1, and the recycling rates are presented in Table S4. As expected, the main source of impurities in the feedstock is from the Al layer in back/bottom with 6.82 wt % followed by Ag with 1.54 wt %. We report that Al is almost completely removed (99.6% yield) from the feedstock through alkali (KOH) leaching. Upon successful removal of Al by the KOH solution, a highly pure Si is obtained (98.403 wt %). Despite the high purity of the Si after the first leaching process, the remaining Ag and Pb would potentially interfere with the cycling performance of Si when used as an electrode material in LIBs.

Table 1. ICP-MS Quantification of Silicon, Al, Pb, and Ag

sample condition	Si (wt %)	Al (wt %)	Pb (wt %)	Ag (wt %)
unleached	91.586	6.819	0.044	1.551
partially leached (only KOH solution)	98.403	0.027	0.026	1.544
fully leached (KOH solution then HNO_3 solution)	99.990	0.007	0.001	0.002

Published in : ACS Sustainable Chemistry & Engineering (2020), vol. 8, issue 15, pp. 5868-5879
DOI: 10.1021/acssuschemeng.9b07434
Status : Postprint (Author's version)

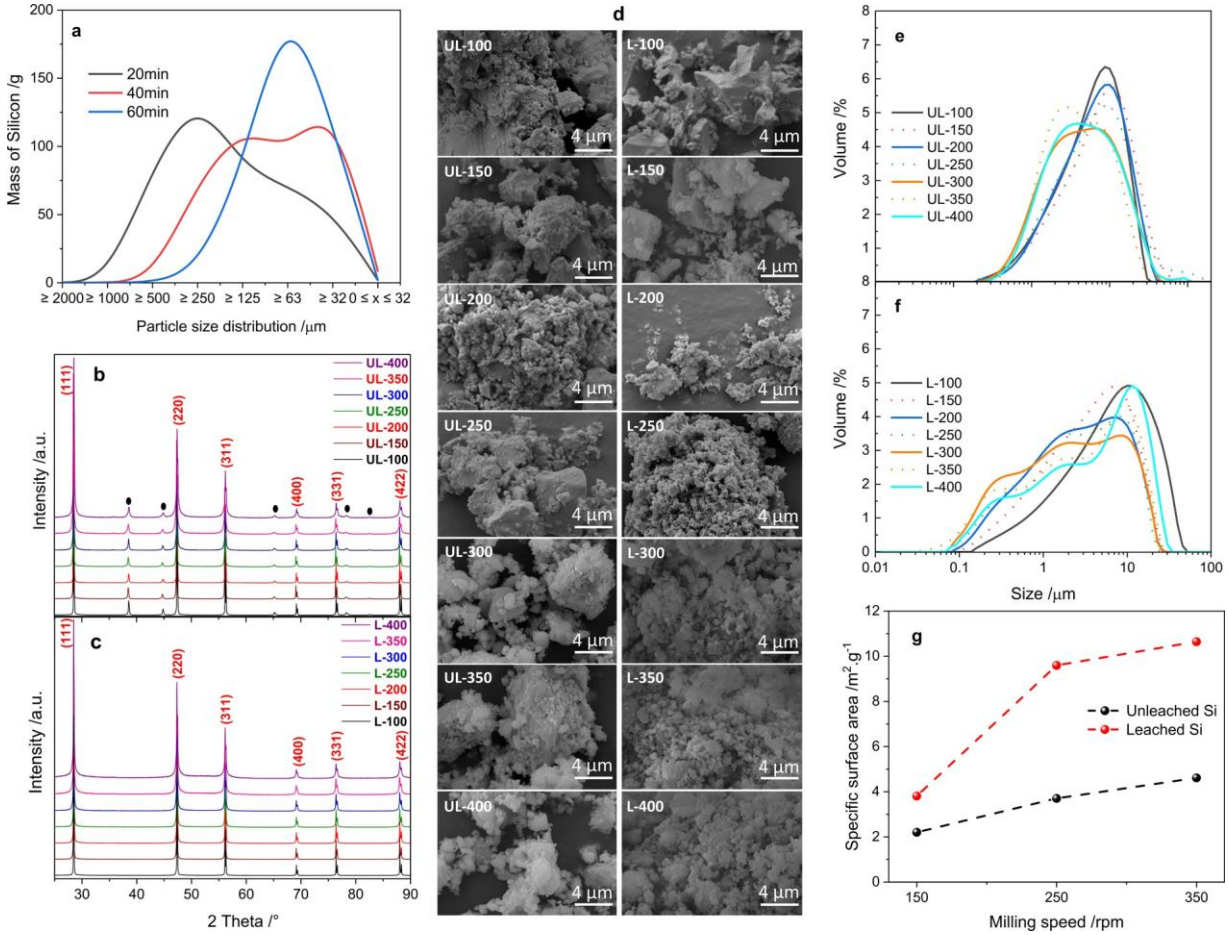

Figure 2. Effect of the ball milling speed on structure and morphology of silicon powders: (a) Evolution of the particle size with milling time in the pregrinding step demonstrates that 60 min of milling is the optimum time to obtain a majority of particles below 125 μm size. (b) XRD patterns of unleached Si after ball milling at different speeds illustrate silicon reflections identified by their (hkl) indices and reflections corresponding to Al and Ag metals marked with black circles. (c) Al and Ag reflections have disappeared in leached powders after ball milling at different speeds, demonstrating the effectiveness of the controlled leaching process. (d) SEM images of unleached Si powder (UL) and leached Si powders (L) after 20 h of milling at different speeds from 100 to 400 rpm illustrates the fact that downsizing in the case of unleached samples is not achieved. (e) Particle-size distribution of unleached Si powder (UL) and (f) leached Si powder (L) after 20 h of milling at different speeds from 100 to 400 rpm demonstrates different distribution behaviors. Size distribution in unleached Si illustrates a well-defined population of large particles in the case of leached powders Si; however, three particle size populations centered at around 0.2−0.3 μm, 1−2 μm, and 8−10 μm are present. (g) The BET specific surface area data further illustrates the difference in efficiency of the milling in unleached and leached Si powders after 20 h of milling at 150, 250, and 350 rpm.

To achieve ultrahigh purity silicon (99.99 wt %), we conducted a second leaching process in a HNO_3 solution. Likewise, Ag is removed via acid leaching (99.87% yield) from the screen-printed layer on top/front. After the completion of the dual bath leaching process, we had a 99.99% recycling rate and purity for the silicon present in PV cells. The resultant silicon is suitable as the starting raw material for fabrication of silicon anodes for Li-ion batteries.

SEM-EDS measurements were done on wafer fragments before and after the leaching process to confirm the results obtained by ICP-MS analysis and demonstrate the successful removal of Al by alkali leaching (Figure S2). The surface layer constituted of an antireflective layer (SiN_x) is removed significantly after leaching, and we have the appearance of pyramid morphology at the surface with well reduced SiN_x content (Figure S3).

Published in : ACS Sustainable Chemistry & Engineering (2020), vol. 8, issue 15, pp. 5868-5879
DOI: 10.1021/acssuschemeng.9b07434
Status : Postprint (Author's version)

Nanosizing of Si for Battery Application.

A two-step process with pregrinding followed by nanosizing was considered. We proceeded with a preliminary grinding step to reduce the Si wafer scraps with large and irregular shapes and to improve the efficiency of the nanosizing step.[30] The pregrinding step is conducted using a tumbling ball mill to transform Si wafer scraps into a coarse powder. The particle size of silicon decreases with an increase in grinding time. Indeed after 60 min, more than 85 wt % of the silicon particles have a particle size lower than 125 μm. The particle size distribution develops a narrow monomodal distribution over time (as shown in Figure 2a).

A secondary grinding step by planetary ball milling was conducted to further reduce the particle size of Si (below 125 μm) due to its simplicity, reproducibility, low cost, and capacity to produce a large amount of material.[39] The milling speed is an important parameter to be considered, and its optimization controls the structural and morphological properties of the particle.[40] The powders were ground at different milling speeds (from 100 to 400 rpm) to determine the optimal milling speed. The procedure was carried out for powders from both leached and unleached Si wafer fragments, to investigate the impact of Al, Ag, and Pb impurities. This grinding step was carried out under an argon atmosphere to avoid the presence of oxygen and oxidation of silicon upon contact with air.[41] SEM-EDS results presented in Figure S4 demonstrate 2.15 atom % of oxygen in the pregrinded powder and 2.18 atom % for the milled powder at 300 rpm (20 h). This oxygen content corresponds to the native oxide layer on silicon after the leaching step. Therefore, we can confirm that no further oxidation is occurring during the ball milling process.

Figure 2b and c present the XRD patterns of unleached (UL-100 to UL-400) and leached (L-100 to L-400) cell fragments ground at different milling speeds (100 to 400 rpm) over 20 h, respectively. All peaks are sharp and well-defined, indicating a high degree of crystallinity of the prepared powders even after the ball milling at high speed (400 rpm). In unleached powder, the main peaks correspond to silicon while Al and Ag metals are detected as minor phases, whereas in leached powders all observed reflections are indexed as silicon and no impurity or secondary phase is detected. In both cases, the peak width increases with increasing the milling speed, which can be interpreted as a decrease in the crystallite size.

We study the influence of Al and Ag on the morphology and specific surface area of unleached Si powders ground at different milling speeds, prior to investigating the impact of these electronically conductive elements (Al and Ag) on the electrochemical performance of the anode in LIB. The particle shape and size does not change much by increasing the milling speed due to the presence of ductile Al and Ag (Figure 2d). The particle-size distribution as shown in Figure 2e exhibits a well-defined population around 8 μm for 100−250 rpm and a polydispersed distribution with a slight increase in the submicrometric fraction for the samples milled at 300, 350, and 400 rpm. These powders have an average size of 3.6−4 μm, showing that nanosizing is not efficient in unleached samples (cumulative volume size distribution and characteristic sizes are shown in Figure S5).

The increase in the milling speed for leached Si powders, however, has a significant impact on the particle shape and size. The SEM images of L-100, L-150, and L-200 samples show large fragments of Si wafers (Figure 2d) that are not ground or slightly ground, but a further increase of the milling speed for leached Si wafers leads to the transformation of Si wafer fragments to submicrometric particles showing a polydispersed size distribution extended from 0.02 to 30 μm with three particle size populations centered at around 0.2−0.3 μm, 1−2 μm, and 8−10 μm. SEM images with higher magnification and TEM images in Figure S6 illustrate that the observed aggregates are constituted of Si nanoparticles. This is in good agreement with the observations made by Gauthier et al.[30] stating that milled silicon powders are nanostructured with micrometric agglomerates.

Published in : ACS Sustainable Chemistry & Engineering (2020), vol. 8, issue 15, pp. 5868-5879
DOI: 10.1021/acssuschemeng.9b07434
Status : Postprint (Author's version)

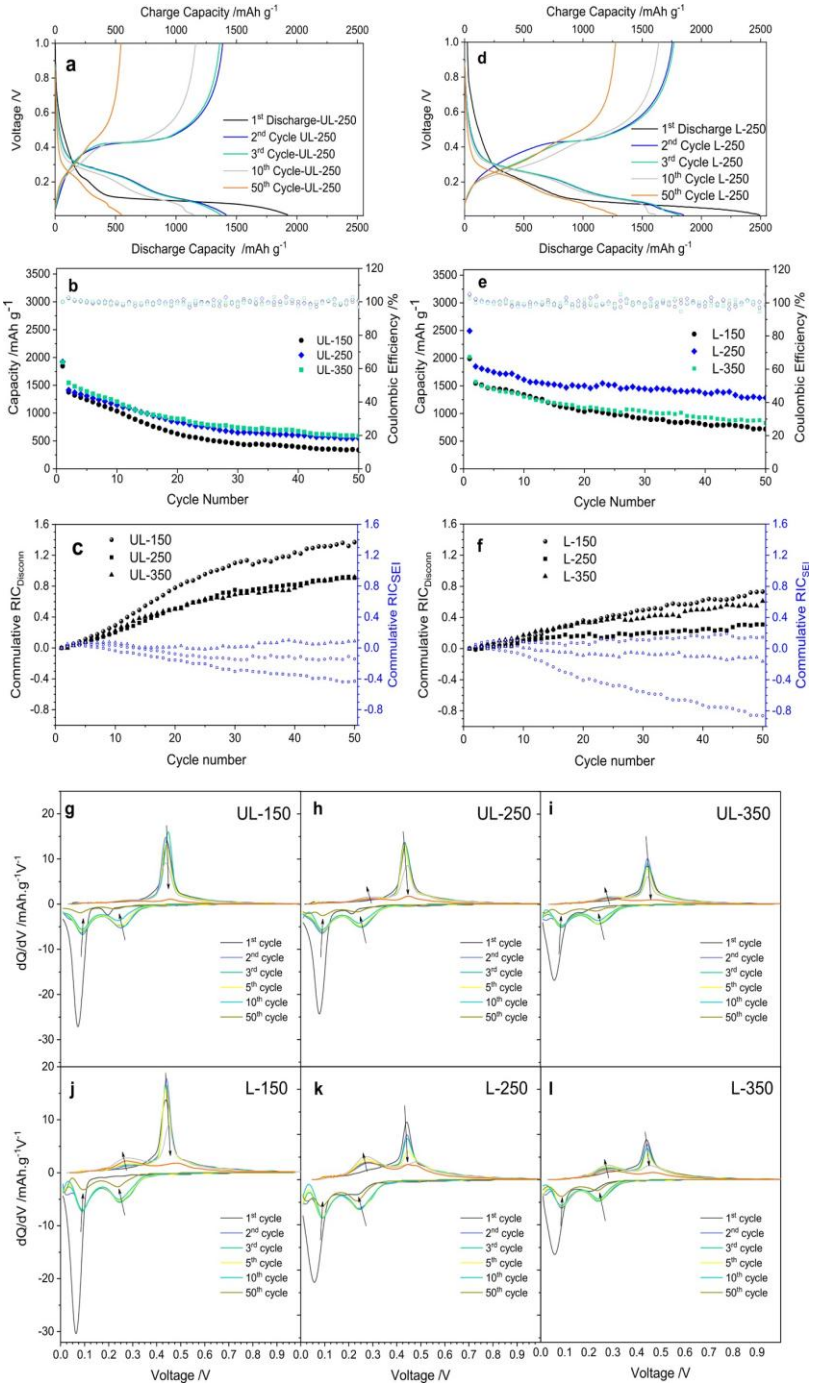

Figure 3. Cycling performance for unleached and leached Si powder with regard to the ball milling speed (potential range explored was 0.01−1 V vs Li^+/Li^0): (a) voltage profile data for first, second, third, 10th, and 50th cycles of UL-250 demonstrate clearly the irreversible capacity loss of the first cycle and the position of charge and discharge plateaus. (b) Evolution of discharge capacity vs cycle number at 0.05C of unleached Si based electrode materials ball milled at different speeds illustrates similar capacity values and capacity losses over time. (c) Cumulated relative irreversible capacities related to disconnection (black) and to the SEI (blue), for unleached Si based electrode materials at different ball milling speeds illustrating a major contribution for the irreversible capacity loss due to disconnection. (d) Voltage profile data for first, second, third, 10th, and 50th cycles of L-250 illustrate a clear plateau at around 0.27 V for charge resulting in higher capacity retention of the material. (e) Evolution of discharge capacity vs cycle number at 0.05C of leached Si based electrode materials ball milled at different speeds illustrates more stable capacity values due to more effective downsizing and also (f) lower contributions in the irreversible capacity loss due to disconnection. Differential capacity discharge/charge curves of (g) UL-150, (h) UL-250, (i) UL-350, (j) L-150, (k) L-250, and (l) L-350 for first, second, third, fifth, 10th, and 50th cycles illustrate the increase/decrease in peak intensity and displacements of the peaks corresponding to the plateaus presented in (a, d) the type of reaction taking place in the electrode.

Published in : ACS Sustainable Chemistry & Engineering (2020), vol. 8, issue 15, pp. 5868-5879
DOI: 10.1021/acssuschemeng.9b07434
Status : Postprint (Author's version)

Figure 2g illustrates the results for BET surface area measurements carried out for unleached and leached Si powders. We observe a slow increase in the surface area (2.2 to 4.6 $m^2 g^{-1}$) for unleached samples and a significant increase in values for leached samples (3.8 to 10.5 $m^2 g^{-1}$) as the milling speed is increased, which is in accordance with the evolution of downsizing in unleached and leached samples.

Effect of The Ball Milling Speed on Electrochemical Properties of Silicon Powders.

In this section, electrochemical performances of the ground powders were assessed by galvanostatic charge−discharge cycling in half-cell configuration in the voltage range 0.01−1 V vs Li^+/Li^0. Charge−discharge cycling of unleached (UL-150 to UL-350) and leached (L-150 to L-350) Si wafer fragments ground at different speeds (from 150 to 350 rpm) for 20 h are presented and compared.

Figure 3a,b presents the voltage profiles (delithiation/lithiation) and cycling performances of the electrodes based on unleached ball-milled wafers. First, a decrease of the voltage to 0.3 V with a capacity of 250 mAh g^{-1} for U-250 without a well-defined plateau is observed, which is due to the SEI (solid electrolyte interphase) layer formation at around 0.7−0.9 V at the surface of the carbon particles used as the conductive additive. It is well-known that at potentials below 1 V, the SEI layer will be formed on the surface of the electrode.[42]

As shown further in Figure 3a, lithiation of silicon occurs in the 0−0.3 V range. During the first lithiation process (discharge), Li will form a Li_xSi alloy, and a sloping voltage profile is observed with a plateau around 0.1 V vs Li^+/Li^0, indicating a two-phase reaction (crystalline Si + amorphous Li_xSi).[43,44] This is followed by a slope change at the end of the discharge profile at about 0.06 V, which is reported to be due to the rapid crystallization of the amorphous Li_xSi phase to $Li_{3.75}Si$.[30] The voltage plateau for discharge increases toward 0.2−0.3 V in the next lithiation steps. The SEI layer formed during the first lithiation will be affected by the volume changes generated upon subsequent lithiation/delithiation processes, and if it is not controlled the SEI layer will break down and create fresh silicon exposed to electrolyte.[42] The combination of the initially formed SEI layer and the SEI formed on freshly exposed silicon will result in the formation of a thick SEI layer. During the delithiation step, the potential increases to about 0.425 V where a single plateau is observed in the voltage profile representing a two-phase region (crystalline $Li_{3.75}Si$ and amorphous Li_ySi) followed by an upwardly sloping region, suggestive of a single-phase solid solution region (amorphous Li_ySi to amorphous Si).[30,43,44]

In general, micrometer-sized silicon particles demonstrate large volume expansion in subsequent cycles and lose capacity due to electrode pulverization.[45] Liu et al. suggested that a critical silicon particle diameter of 150 nm is needed to prevent surface crack initiation due to high expansion of particles upon first lithiation, which eventually can cause fractures and failure in electrodes.[45,46] Indeed, as shown in Figure 3b, there is considerable capacity loss in unleached Si samples in which the downsizing of particle size was less efficient (Figure 2e) and low specific surface area was reported (Figure 2g). Similar influence of size and specific surface area in case of Si nanowires is reported by Hansen et al.[47] The discharge capacity values for UL-150, UL-250, and UL-350 over the first 50 cycles are shown in Figure 3b as an example. For UL-150, where we observe dense particles (Figure 2d), the capacity loss is larger after 10 cycles as compared to the results of UL-250 and UL-350. This is also observed in the voltage profiles in Figure S7. The voltage plateaus for lithiation and delithiation at different cycles (Figure S7, Figure S8a) are similar for all samples. The discharge capacity retention values for UL-150, UL-250, and UL-350 are 25.5%, 40.08%, and 39.75% after 50 cycles, respectively.

Published in : ACS Sustainable Chemistry & Engineering (2020), vol. 8, issue 15, pp. 5868-5879
DOI: 10.1021/acssuschemeng.9b07434
Status : Postprint (Author's version)

To understand the contribution of disconnection (loss of electrical contact between particles) and formation of the SEI layer on capacity loss in Si electrodes, cumulated relative irreversible capacities of the samples are considered. RIC_D, representing the relative irreversible capacity associated with the disconnection of particles, and RIC_{SEI}, representing the irreversible capacity related to the SEI formation, are calculated using the following formulas (eqs 5 and 6):[30]

$$RIC_D = \frac{C_{Cn} - C_{Cn+1}}{C_{Cn}} \quad (5)$$

$$RIC_{SEI} = \frac{C_{Dn+1} - C_{Cn}}{C_{Cn}} \quad (6)$$

As presented in Figure 3c, the cumulative RIC_D is similar for UL-150, UL-250, and UL-350 negative electrodes in the first 10 cycles, but after subsequent cycling, the UL-150 anode exhibits an increase in RIC_D and the cumulated value shows an increased slope as compared to UL-250 and UL-350 samples, which have similar values. This is in agreement with the results shown in Figure 3b that display the evolution of the discharge capacity with cycle number. The evolution of the irreversible capacity related to the SEI formation (RIC_{SEI}) shows no difference between unleached samples at different milling speeds in the first 15 cycles (Figure 3c). The capacity corresponding to the formation of the SEI is obtained from the difference in C_{Dn+1} and C_{Cn} and after the first 15 cycles remains relatively stable in UL-350. For UL-150 and UL-250, the cumulative RIC_{SEI} exhibits negative values, thus showing no contribution of Li consumption to the formation of SEI. The combined effect of pulverization (increase in RIC_D) and the formation of unstable SEI results in capacity loss in unleached samples where the best capacity retention after 50 cycles was 40% for the UL-250 electrode. The differential capacity profiles of unleached samples show a decrease of anodic and cathodic peaks with cycling (Figure 3g–l). Peaks are shifted to lower voltages during the lithiation process (discharge) and to a higher voltage for the peak ca. 4.25 V during the delithiation process in all samples. We also observe a slight peak at around 0.27 V appearing after the first cycle in the delithiation step for UL-250 and UL-350, which will be further discussed in the case of leached samples.

The voltage profile of L-150, L-250, and L-350 for the first discharge (lithiation) and the subsequent charge and discharge are shown in Figure S8. We observe a difference in the shape of the voltage profile for the first lithiation in which distinct plateaus are observed at 0.07 V for L-150 and start to have a sloping curve starting from 0.3 V in L-250 and 0.25 V in L-350. Such a behavior is often reported when Si particle size is less than 20 nm.[43] Gauthier et al. reported that since the proportion of amorphous interfacial regions in milled powders is relatively high, the electrochemical behavior of nanostructured micrometric Si powders is similar to nanometric Si powders.[30] The differential capacity profile in Figure 3g–l also presents two peaks below 0.3 V for the first lithiation in L250 and L-350, while the main peak is similar to L-150 at around 0.07 V. The voltage profile of the most promising electrode (L-250) is presented in Figure 3d, with two subsequent discharge−charge curves after the first lithiation, the 10th and 50th cycles. We observe a high irreversible capacity loss for the first cycle, but after formation of the SEI layer the subsequent cycles show Coulombic efficiency (CE) values near 100%. The cycling performances of leached samples at different speeds are also compared in Figure 3e. The first lithiation for L-250 at 0.05C shows a capacity of 2500 mAh g^{-1} as compared to 2000 mAh g^{-1} for the L-150 and L-350 samples. After the first lithiation and capacity loss due to SEI formation, the L-150, L-250, and L-350 samples show capacity retentions of 47.34%, 71.0%, and 55.36% after 50 cycles, respectively.

Published in : ACS Sustainable Chemistry & Engineering (2020), vol. 8, issue 15, pp. 5868-5879
DOI: 10.1021/acssuschemeng.9b07434
Status : Postprint (Author's version)

The evolution of cumulated RIC_D and RIC_{SEI} is quite different in leached Si samples compared to unleached ones. As presented in Figure 3f, the evolution of cumulative RIC_D for L150, L-250, and L-350 is similar in the first 15 cycles, and after that the irreversibility associated with the disconnection of particles in L-250 is half of the value compared to L-150 and L-350. This could be due to the smaller particle size of L-250 compared to L-150 and lower aggregation of Si particles with a lower proportion of amorphous interfacial regions in L-250 compared to L-350. The L-250 electrode consists of nanoparticles and agglomerates of submicrometric particles mixed with carbon and CMC (as presented in Figure S9a). The electrode mixture enables the expansion of Si particles upon lithiation (Figure S9b) while keeping the connection between the particles. After delithiation (Figure S9c), the contact between the mixture components was preserved, in agreement with lower RIC_D values. The cumulated RIC_{SEI} of L-250 is quite stable and does not increase gradually for the 50 cycles, which can be the result of the formation of a stable SEI layer which gives very good capacity retention after 50 cycles with a high capacity of 1285 mAh g^{-1} (Figure 3e,f). The evolution of RIC_{SEI} in L-150 and L-350 shows that they are not contributing to Li consumption to form SEI, but mainly the disconnection of particles results in capacity loss.

The major difference in differential capacity profiles of leached and unleached samples is the presence and increase in the height of the peak at 0.27 V for delithiation in all samples shown in Figure 3g–l. The delithiation at 0.27 V corresponds to the conversion of crystalline $Li_{3.75}Si$ to amorphous Li_xSi ($x \sim 2$) and the delithiation around 0.425 V corresponds to a single-phase solid solution region (amorphous Li_ySi to amorphous Si).[43,44,48] The evolution of the differential capacity profiles upon cycling in L-150, L-250, and L-350 clearly shows that a higher peak ratio for delithiation at 0.27 V compared to delithiation at 0.425 V will result in higher capacity retention over time, because the decrease in the peak at 0.425 V must be compensated by an increase of the peak at 0.27 V in order to satisfy the capacity requirement.[49] However, for unleached powders, the increase in intensity of the peak at 0.27 V with cycling is not significant, which demonstrates the presence of lower or no crystalline $Li_{3.75}Si$ content related to the reactions of Li with unleached materials, leading to low capacity retention compared to the leached samples.

Effect of the Ball Milling Duration and BPR Ratio on the Structural And Morphological Properties Of Silicon Powders.

Different parameters such as vial volume, ball size, total ball mass, milling (rotational) speed, powder quantity, atmosphere, and milling time can strongly affect the results in planetary ball mills.[40,50] In this section, the influence of milling time with a ball to powder (BPR) ratio of 5:1 on particle size and the

Published in : ACS Sustainable Chemistry & Engineering (2020), vol. 8, issue 15, pp. 5868-5879
DOI: 10.1021/acssuschemeng.9b07434
Status : Postprint (Author's version)

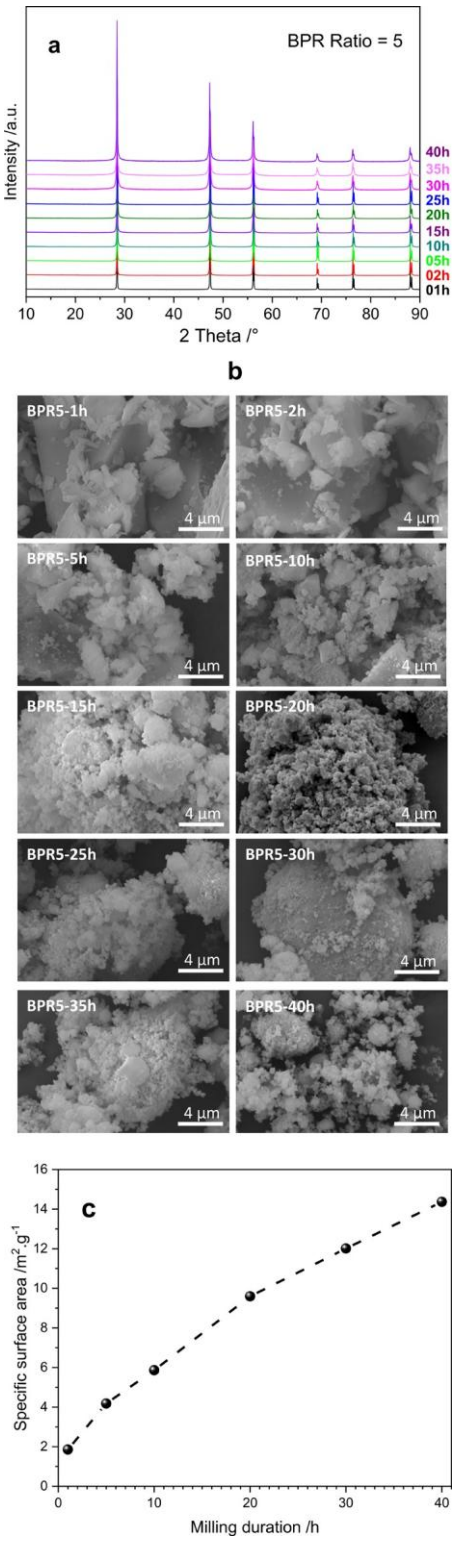

Figure 4. Effect of the ball milling duration on the structure and morphology of silicon powders: (a) Similar XRD patterns were obtained for all the milled powders with BPR = 5 showing similar diffraction patterns with sharp peaks. (b) SEM images of the recovered silicon milled during different durations which ranged from 1 to 40 h for BPR = 5 show a decrease of size with the appearance of agglomerated submicrometric particles over time. (c) BET specific surface area of Si powder milled at 250 rpm for different milling durations from 1 h to 40 h illustrates a linear increase of the specific surface area with milling time.

Published in : ACS Sustainable Chemistry & Engineering (2020), vol. 8, issue 15, pp. 5868-5879
DOI: 10.1021/acssuschemeng.9b07434
Status : Postprint (Author's version)

morphology of leached silicon wafers is investigated. The results demonstrating the influence of milling time with a BPR of 10:1 is presented in the Supporting Information (Figures S10−12). Powder XRD patterns of the silicon milled at 250 rpm during different durations which ranged from 1 to 40 h are shown in Figure 4a. All ground samples show similar diffraction patterns and sharp peaks due to their highly crystalline structure of silicon powders. Changes in the relative peak position and peak widths were observed for the milled samples compared with the baseline sample. Indeed, the low increment of broadening effect at the peak base is observed with an increase in the duration of milling, which corresponds to the reduction of the particle size of silicon mainly at long duration.

Figure 4b shows the SEM images of the silicon milled during different durations (1 to 40 h) at 250 rpm with a BPR of 5:1. In the beginning of the milling (0−10 h), dense particles and, after longer milling times (10−40 h), agglomerates are observed. Indeed, the particle-size distribution of these samples (Figure S11) exhibits a rather defined population around 10 μm which grows to form a polydispersed distribution upon increasing of the grinding duration to 10 h. The particles after 10 h milling and onward are composed of submicrometric fractured platelets that are forming agglomerates. The characteristic sizes (d_{10}, d_{50}, and d_{90}) of Si powders milled during different durations (1 to 40 h) with a BPR of 5:1 are shown in Figure S12, where we observe that the particle size is decreasing efficiently during the first 10 h of milling and reaches more or less a plateau at around 3 μm. This plateau gives the size of the agglomerates from submicrometric Si particles. The more or less linear increase in specific surface area from 1 to 40 h as represented in Figure 4c is a result of efficient nanosizing with an increase in milling time.

Effect of the Ball Milling Duration on Electrochemical Properties of Silicon Powders.

This section highlights the electrochemical performance of leached Si wafer fragments ball milled at 250 rpm with different milling durations.

Evolution of discharge capacity vs cycle number for Si-based electrode materials ball milled at different milling durations is presented in Figure 5a. All materials show a high initial capacity of about 2500 mAh g^{-1}, and apart from the Si-5h, all other tested electrodes (10, 20, 30, and 40 h) show a relatively stable capacity of over 1250 mAh g^{-1} after 50 cycles. Cumulated relative irreversible capacities relative to disconnection and to the SEI are also presented in Figure 5b, where after 15 cycles the contribution of RIC_D is lower for Si-10h to Si-40h electrodes as compared to Si-5h in which larger particles and aggregations are present, thus the electrochemical performances of Si-10 to Si-40 samples are superior to those of Si-5h. This is in agreement with the characteristic sizes (d_{10}, d_{50}, and d_{90}) of Si milled for different durations (1 to 40 h) at 250 rpm, illustrating the presence of smaller particles in these samples (Figure S12) and also with the BET surface area presented in Figure 4c. Voltage profiles corresponding to the lithiation and delithiation of silicon with different milling durations are presented in Figure 5c−e. Similar to samples with different milling speeds, the first lithiation in Si-5h to Si-40h samples exhibits a distinct flat plateau around 0.1 V and voltage profiles are affected by Si particle size resulting in round-shaped curves with lithiation taking place in the 0−0.3 V range. We observe more defined plateaus for delithiation in the second cycle (Figure 5c) that remain around the same voltage range after 50 cycles (Figure 5d). This is also supported by the evolution of differential capacity profiles for charge/discharge shown in Figure 5f−j. The presence of these two plateaus corresponding to the reactions leading to transformation of Si to $Li_{3.75}Si$ is favorable (as mentioned before) since higher capacity value and improved capacity retention are observed for Si anodes upon formation of amorphous Li_xSi and later on formation of crystalline $Li_{3.75}Si$. The presence of submicrometric and nanoparticles contributes to the formation of a stable SEI layer and better contacts which inhibit the irreversible capacity due to disconnection.[30] The voltage profile of Si-10h upon subsequent cycling is presented as an example to illustrate the difference in the form of the delithiation curve (Figure 5e).

Published in : ACS Sustainable Chemistry & Engineering (2020), vol. 8, issue 15, pp. 5868-5879
DOI: 10.1021/acssuschemeng.9b07434
Status : Postprint (Author's version)

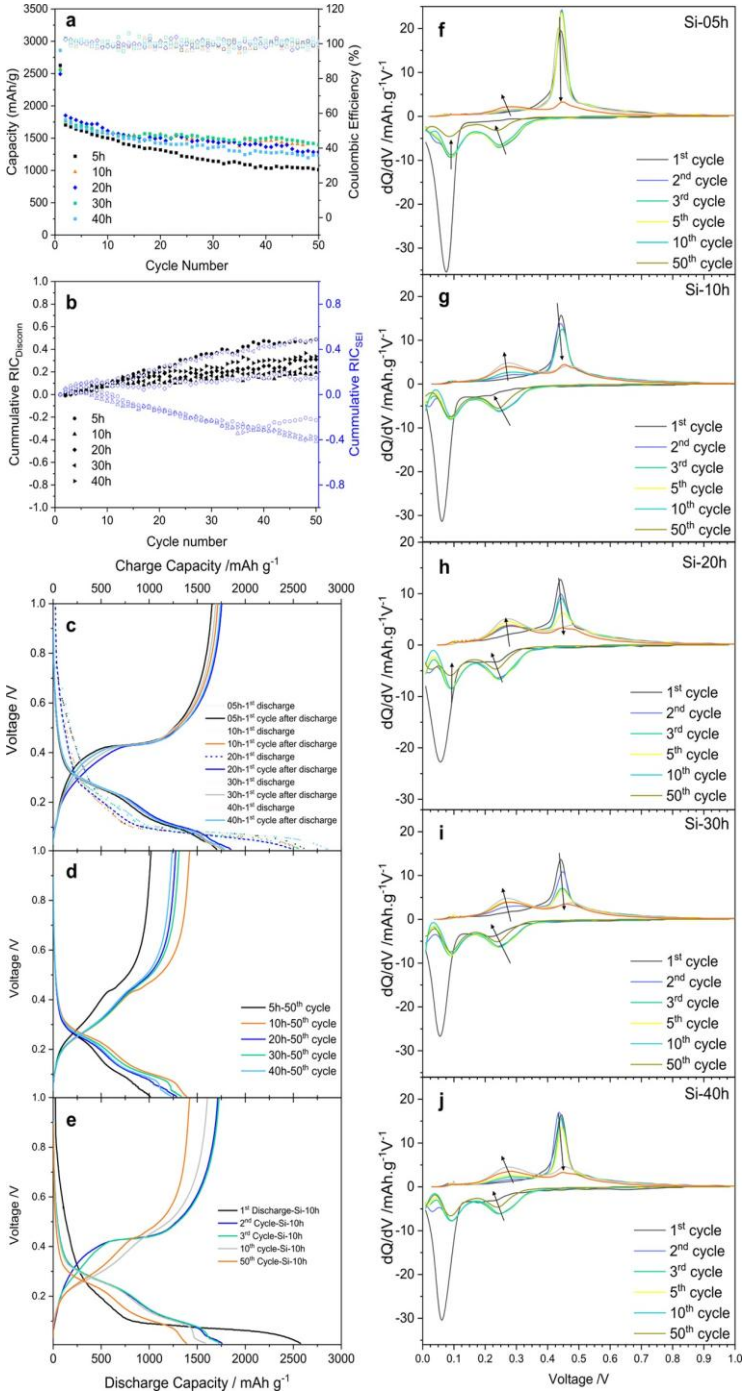

Figure 5. Cycling performance of Si powder with different ball milling durations (BPR = 5 and potential range explored was 0.01−1 V vs Li^+/Li^0): (a) Evolution of discharge capacity vs cycle number at 0.05C illustrating the capacity retention over time for Si powders ball milled during different milling times. (b) Cumulated relative irreversible capacities relative to disconnection (black) and to the SEI (blue), of Si based electrode materials ball milled for different milling durations, demonstrating the saturation of the disconnection component as milling duration increases. (c) Voltage profiles of the first lithiation and delithiation cycles for Si powders with different milling durations demonstrating similar voltage plateaus with small difference for the delithiation plateau near 0.3 V. (d) Voltage profile data of the 50th cycle of the recovered Si ball milled with different milling durations demonstrating that increasing the milling duration to 10 h and onward can ensure a high capacity value of above 1250 mAh g^{-1} and (e) voltage profile data of the first, second, third, 10th, and 50th cycles of the Si-10h sample (ball milled at 250 rpm for 10 h) at 0.05C illustrating the first voltage plateau upon lithiation and the slope changes in the voltage plateaus upon subsequent cycling. Differential capacity discharge/charge curves of (f) Si-5h, (g) Si-10h, (h) Si-20h, (i) Si-30h, and (j) Si-40h for the first, second, third, 10th, and 50th cycles demonstrate that after the first cycles, the intensity of the peak around 0.27 V is increased, and at the same time the intensity of the peak at 0.425 V decreases. This behavior improves the reversible capacity of the cell.

Published in : ACS Sustainable Chemistry & Engineering (2020), vol. 8, issue 15, pp. 5868-5879
DOI: 10.1021/acssuschemeng.9b07434
Status : Postprint (Author's version)

The delithiation starts with a round curve followed by a rather defined plateau at around 0.425 V. As shown in Figure 5f–j after the first cycles, the intensity of the peak around 0.27 V is increased, and at the same time the intensity of the peak at 0.425 V decreases, meaning that conversion of crystalline $Li_{3.75}Si$ to amorphous Li_xSi is contributing the most to the reversible capacity of the cell.

A milling duration of 10 h is necessary to reach a plateau in the particle size values as shown in Figure S12. The average particle size in this case is around 3 µm after 10 h of milling. We also detected nanometric and sub-micrometric particles in the size distribution profile (Figure S11), which can create bridging points between the larger particles or aggregates to ensure the electronic conductivity and inhibit the pulverization in the electrodes during cycling. We demonstrated that even though the particle sizes of silicon which was recovered from solar cells are quite large, capacity retentions of 61.15%, 81.6%, 71.0%, 81.95%, and 71.47% were obtained for Si-5h, Si-10h, Si20h, Si-30h, and Si-40h, respectively. In order to improve these results, one approach could be to use a milling setup providing higher energy to decrease the particles size further or to prepare Si/C composite powders where the carbon will act as a buffer layer and improve the electrical conductivity further.

Sustainability of the System.

Fabrication of solar-grade silicon is extremely energy-intensive due to its ultrahigh purity. It is noteworthy that the most energy-intensive step in the production of silicon modules is the Siemens process, which converts $SiHCl_3$ to ultrapure silicon. Annual end-of-life PV panel waste is projected to increase to more than 60−78 million metric tons cumulatively by 2050.[51] As such, recovering silicon from the modules could lead to significant energy savings and result in the introduction of value-added applications for silicon.

This work relates to the high-added-value product of recovered silicon, meaning the silicon anode in lithium ion batteries. Table S5 illustrates the superior electrochemical performance of the recovered Si investigated in this work as compared to commercial/synthesized silicon anode material for LIBs. The leaching and nanosizing process discussed in this work along with the development of silicon anodes using recycled Si could be considered a sustainable technology.

Conclusions

To date, chemical routes used for recycling the end-of-life photovoltaic (PV) panels predominantly use harmful HF for leaching and have been evaluated simply on the basis of their ability to separate valuable components in PVs. It is shown in this paper that a HF-free recovery process can be deployed to obtain silicon with value-added applications in Li-ion batteries. Our silicon recovery route consisted of removing connections and conductive layers present in photovoltaic cells followed by ball milling to obtain ultrahigh purity nanosized Si powder as a green and energy-efficient Si source. Comparison of the electrochemical performance of leached and unleached samples confirmed that the leaching step is essential, since Al and Ag residues prevent the efficient down-sizing of the Si particles during ball milling. Structural and morphological properties of Si powders as well as their electrochemical performances as a function of milling speed and duration have been explored. Si wafer fragments after ball milling exhibit a broad size distribution profile with nanometric to micrometric particles while preserving the crystalline structure. A milling speed of 250 rpm and at least 10 h milling duration were found necessary to improve the

performance of batteries. High capacity retentions over time are supported by the decreased relative irreversible capacity when ball milling with sufficient energy (milling speed) and time was conducted, resulting in a capacity of around 1400 mAh g^{-1}. High capacity values obtained for Si powders are associated with the presence of connected nanometric and micrometric particles which create a network accommodating conductive carbon particles and a binder in the electrode preparation step. A stable SEI layer is formed upon subsequent cycling, and the main phase transition process after a few cycles during charge (delithiation) is associated with the conversion of crystalline $Li_{3.75}Si$ to amorphous Li_xSi, which results in reversible lithiation of Si particles to form crystalline $Li_{3.75}Si$ (<0.1 V), thus promoting higher capacity values with cycling. We expect that our proposed platform for value-added recovery of Si from PV wastes to be repurposed and used in lithium-ion batteries will cover general interest and find application in other technologies where high-quality inexpensive Si is required.

Associated content

Supporting Information is available free of charge at https://pubs.acs.org/doi/10.1021/acssuschemeng.9b07434 .
Details of leaching bath composition, time, and temperature optimization with corresponding ICP-MS results; overview of chemical methods for recovery of metals from photovoltaic panels; Figures S1−S3, SEM images and SEM/EDS results of silicon wafer before and after leaching steps; Figure S4, SEM/EDS results of pregrinded and milled powders; Figure S5, cumulative volume size distribution and characteristic sizes of unleached and leached Si milled at different speeds; Figure S6, SEM and TEM images of L-250 sample; Figures S7 and S8, voltage profile of unleached and leached Si samples; Figure S9, SEM images of leached Si based electrodes before cycling, after lithiation, and after delithiation; Figure S10, effect of ball milling duration with BPR ratio = 10; Figure S11, particle size distribution of Si powder with different ball milling durations; Figure S12, evolution of the characteristic sizes of Si milled during different durations (PDF)

Acknowledgments

N.E. is a FRIA grantee [Grant 1.E118.16] of the Fonds de la Recherche Scientifique − FNRS. This work was supported by the Walloon Region through the Beware Fellowship Academia [2015-1, RESIBAT no. 1510399] and SOLARCYCLE project [Grant agreement no. 6841]. Part of this work was supported by the Walloon Region under the "PE PlanMarshall2.vert" program (BATWAL − 1318146).

References

(1) Padoan, F. C. S. M.; Altimari, P.; Pagnanelli, F. Recycling of End of Life Photovoltaic Panels: A Chemical Prospective on Process Development. Sol. Energy 2019, 177, 746−761.
(2) Weckend, S.; Wade, A.; Heath, G. End-of-Life Management: Solar Photovoltaic Panels; International Renewable Energy Agency (IRENA) and International Energy Agency Photovoltaic Power Systems Programme, 2016.
(3) PV CYCLE. PV Waste & Legislation. http://www.solarwaste. eu/pv-waste-legislation/ (accessed Dec 3, 2018).
(4) Schrijnemakers, A.; Fredé rić Boschini, R. C. Method for Recycling Photovoltaic Solar Cells Module, Patent EP3323150, 2017.
(5) Jung, B.; Park, J.; Seo, D.; Park, N. Sustainable System for RawMetal Recovery from Crystalline Silicon Solar Panels: From NobleMetal Extraction to Lead Removal. ACS Sustainable Chem. Eng. 2016, 4 (8), 4079−4083.
(6) Chen, Z.; You, Y.; Morita, K. Sustainable Simultaneous Synthesis of Titanium-Bearing Materials from Silicon Waste and TiO2-Bearing Slag. ACS Sustainable Chem. Eng. 2018, 6 (8), 10742−10750.
(7) Dytrych, P.; Bumba, J.; Kastanek, F.; Fajgar, R.; Kostejn, M.; Solcova, O. Waste Photovoltaic Panels for Ultrapure Silicon and Hydrogen through the Low-Temperature Magnesium Silicide. Ind. Eng. Chem. Res. 2017, 56 (45), 12863−12869.
(8) Yi, Y. K.; Kim, H. S.; Tran, T.; Hong, S. K.; Kim, M. J. Recovering Valuable Metals from Recycled Photovoltaic Modules. J. Air Waste Manage. Assoc. 2014, 64 (7), 797−807.

(9) Hoffmann, M.-C.; Suitner, H.; Thomas, R. H2020 CABRISS Public Business Plan; Zenodo, 2017, DOI: 10.5281/zenodo.998558.

(10) Yousef, S.; Tatariants, M.; Denafas, J.; Makarevicius, V.; Lukosiu̅te, S. I.; Kruopienė , J̇ . Sustainable Industrial Technology for Recovery of Al Nanocrystals, Si Micro-Particles and Ag from Solar Cell Wafer Production Waste. Sol. Energy Mater. Sol. Cells 2019, 191, 493−501.

(11) Yousef, S.; Tatariants, M.; Tichonovas, M.; Makarevicius, V. Sustainable Technology for Mass Production of Ag Nanoparticles and Al Microparticles from Damaged Solar Cell Wafers. Waste Manage. 2019, 98, 126−134.

(12) Huang, X.; Pu, H.; Chang, J.; Cui, S.; Hallac, P. B.; Jiang, J.; Hurley, P. T.; Chen, J. Improved Cyclic Performance of Si Anodes for Lithium-Ion Batteries by Forming Intermetallic Interphases between Si Nanoparticles and Metal Microparticles. ACS Appl. Mater. Interfaces 2013, 5 (22), 11965−11970.

(13) Tamirat, A. G.; Hou, M.; Liu, Y.; Bin, D.; Sun, Y.; Fan, L.; Wang, Y.; Xia, Y. Highly Stable Carbon Coated Mg2Si Intermetallic Nanoparticles for Lithium-Ion Battery Anode. J. Power Sources 2018, 384, 10−17.

(14) Wang, G. X.; Sun, L.; Bradhurst, D. H.; Zhong, S.; Dou, S. X.; Liu, H. K. Innovative Nanosize Lithium Storage Alloys with Silica as Active Centre. J. Power Sources 2000, 88 (2), 278−281.

(15) Obrovac, M. N. Si-Alloy Negative Electrodes for Li-Ion Batteries. Curr. Opin. Electrochem. 2018, 9, 8−17.

(16) Chew, S. Y.; Guo, Z. P.; Wang, J. Z.; Chen, J.; Munroe, P.; Ng, S. H.; Zhao, L.; Liu, H. K. Novel Nano-Silicon/Polypyrrole Composites for Lithium Storage. Electrochem. Commun. 2007, 9 (5), 941−946.

(17) Uchida, S.; Yamagata, M.; Ishikawa, M. Effect of Electrolyte Additives on Non-Nano-Si Negative Electrodes Prepared with Polyimide Binder. J. Electrochem. Soc. 2015, 162 (3), A406−A412.

(18) Park, S. J.; Zhao, H.; Ai, G.; Wang, C.; Song, X.; Yuca, N.; Battaglia, V. S.; Yang, W.; Liu, G. Side-Chain Conducting and PhaseSeparated Polymeric Binders for High-Performance Silicon Anodes in Lithium-Ion Batteries. J. Am. Chem. Soc. 2015, 137 (7), 2565−2571.

(19) Wang, B.; Li, X.; Zhang, X.; Luo, B.; Zhang, Y.; Zhi, L. ContactEngineered and Void-Involved Silicon/Carbon Nanohybrids as Lithium-Ion-Battery Anodes. Adv. Mater. 2013, 25 (26), 3560−3565.

(20) Li, X.; Meduri, P.; Chen, X.; Qi, W.; Engelhard, M. H.; Xu, W.; Ding, F.; Xiao, J.; Wang, W.; Wang, C.; et al. Hollow Core-Shell Structured Porous Si-C Nanocomposites for Li-Ion Battery Anodes. J. Mater. Chem. 2012, 22 (22), 11014−11017.

(21) Wu, H.; Yu, G.; Pan, L.; Liu, N.; McDowell, M. T.; Bao, Z.; Cui, Y. Stable Li-Ion Battery Anodes by in-Situ Polymerization of Conducting Hydrogel to Conformally Coat Silicon Nanoparticles. Nat. Commun. 2013, 4, 1943−1946.

(22) Luo, J.; Zhao, X.; Wu, J.; Jang, H. D.; Kung, H. H.; Huang, J. Crumpled Graphene-Encapsulated Si Nanoparticles for Lithium Ion Battery Anodes. J. Phys. Chem. Lett. 2012, 3 (13), 1824−1829.

(23) Liu, N.; Lu, Z.; Zhao, J.; Mcdowell, M. T.; Lee, H. W.; Zhao, W.; Cui, Y. A Pomegranate-Inspired Nanoscale Design for LargeVolume-Change Lithium Battery Anodes. Nat. Nanotechnol. 2014, 9 (3), 187−192.

(24) Bang, B. M.; Lee, J. I.; Kim, H.; Cho, J.; Park, S. HighPerformance Macroporous Bulk Silicon Anodes Synthesized by Template-Free Chemical Etching. Adv. Energy Mater. 2012, 2 (7), 878−883.

(25) Ohara, S.; Suzuki, J.; Sekine, K.; Takamura, T. A Thin Film Silicon Anode for Li-Ion Batteries Having a Very Large Specific Capacity and Long Cycle Life. J. Power Sources 2004, 136, 303−306.

(26) Esmanski, A.; Ozin, G. A. Silicon Inverse-Opal-Based Macroporous Materials as Negative Electrodes for Lithium Ion Batteries. Adv. Funct. Mater. 2009, 19 (12), 1999−2010.

(27) Wang, J.; Yang, J.; Lu, S. A Mini Review: Nanostructured Silicon-Based Materials for Lithium Ion Battery. Nanosci. Nanotechnol.–Asia 2016, 6 (1), 3−27.

(28) Chan, C. K.; Peng, H.; Liu, G.; Mcilwrath, K.; Zhang, X. F.; Huggins, R. A.; Cui, Y. High-Performance Lithium Battery Anodes Using Silicon Nanowires There Is Great Interest in Developing Rechargeable Lithium Batteries with Higher Energy Capacity and Longer Cycle Life for Applications in Portable Electronic Devices, Electric Vehicles and I. Nature Nanotechnology 2007, 31−35, DOI: 10.1038/nnano.2007.411.

(29) Gauthier, M.; Reyter, D.; Mazouzi, D.; Moreau, P.; Guyomard, D.; Lestriez, B.; Roue, Ĺ . From Si Wafers to Cheap and Efficient Si Electrodes for Li-Ion Batteries. J. Power Sources 2014, 256, 32−36.

(30) Gauthier, M.; Mazouzi, D.; Reyter, D.; Lestriez, B.; Moreau, P.; Guyomard, D.; Roue, Ĺ. A Low-Cost and High Performance BallMilled Si-Based Negative Electrode for High-Energy Li-Ion Batteries. Energy Environ. Sci. 2013, 6 (7), 2145−2155.

(31) Klugmann-Radziemska, E.; Ostrowski, P.; Drabczyk, K.; Panek, P.; Szkodo, M. Experimental Validation of Crystalline Silicon Solar Cells Recycling by Thermal and Chemical Methods. Sol. Energy Mater. Sol. Cells 2010, 94 (12), 2275−2282.
(32) Park, J.; Park, N. RSC Advances Wet Etching Processes for Recycling Crystalline Silicon Solar Cells from End-of-Life Photovoltaic Modules. RSC Adv. 2014, 4, 34823−34829.
(33) Klugmann-Radziemska, E.; Ostrowski, P. Chemical Treatment of Crystalline Silicon Solar Cells as a Method of Recovering Pure Silicon from Photovoltaic Modules. Renewable Energy 2010, 35 (8), 1751−1759.
(34) Kang, S.; Yoo, S.; Lee, J.; Boo, B.; Ryu, H. Experimental Investigations for Recycling of Silicon and Glass from Waste Photovoltaic Modules. Renewable Energy 2012, 47, 152−159.
(35) Takami, K.; Kobashi, M.; Shiraga, Y.; Uddin, M. A.; Kato, Y.; Wu, S. Effect of HF and HNO3 Concentration on Etching Rate of Each Component in Waste Crystalline Silicon Solar Cells. Mater. Trans. 2015, 56 (12), 2047−2052.
(36) Park, J.; Kim, W.; Cho, N.; Lee, H.; Park, N. An Eco-Friendly Method for Reclaimed Silicon Wafers from a Photovoltaic Module: From Separation to Cell Fabrication. Green Chem. 2016, 18 (6), 1706−1714.
(37) Yi, R.; Gordin, M. L.; Wang, D. Integrating Si Nanoscale Building Blocks into Micro-Sized Materials to Enable Practical Applications in Lithium-Ion Batteries. Nanoscale 2016, 8 (4), 1834− 1848.
(38) Porciuncula, C. B.; Marcilio, N. R.; Tessaro, I. C.; Gerchmann, M. Production of Hydrogen in the Reaction between Aluminum and Water in the Presence of NaOH and KOH. Braz. J. Chem. Eng. 2012, 29 (2), 337−348.
(39) Russo, L.; Colangelo, F.; Cioffi, R.; Rea, I.; De Stefano, L. A Mechanochemical Approach to Porous Silicon Nanoparticles Fabrication. Materials 2011, 4 (6), 1023−1033.
(40) Nilssen, B. E.; Kleiv, R. A. Silicon Powder Properties Produced in a Planetary Ball Mill as a Function of Grinding Time, Grinding Bead Size and Rotational Speed. Silicon 2020, 21−23.
(41) Emadi Shaibani, M.; Eshraghi, N.; Ghambari, M. Sintering of Grey Cast Iron Powder Recycled via Jet Milling. Mater. Eng. 2013, 47, 174−178.
(42) Mahmoud, A.; Chamas, M.; Lippens, P. E. Electrochemical Impedance Study of the Solid Electrolyte Interphase in MnSn2 Based Anode for Li-Ion Batteries. Electrochim. Acta 2015, 184, 387−391.
(43) Zhang, W. J. Lithium Insertion/Extraction Mechanism in Alloy Anodes for Lithium-Ion Batteries. J. Power Sources 2011, 196 (3), 877−885.
(44) Li, J.; Dahn, J. R. An in Situ X-Ray Diffraction Study of the Reaction of Li with Crystalline Si. J. Electrochem. Soc. 2007, 154 (3), 156−161.
(45) Lee, J. K.; Oh, C.; Kim, N.; Hwang, J. Y.; Sun, Y. K. Rational Design of Silicon-Based Composites for High-Energy Storage Devices. J. Mater. Chem. A 2016, 4 (15), 5366−5384.
(46) Liu, X. H.; Zhong, L.; Huang, S.; Mao, S. X.; Zhu, T.; Huang, J. Y. Size-Dependent Fracture of Silicon. ACS Nano 2012, 6 (2), 1522− 1531.
(47) Hansen, S.; Quiroga-Gonzalez, E.; Carstensen, J.; Adelung, R.; Föll, H. Size-Dependent Physicochemical and Mechanical Interactions in Battery Paste Anodes of Si-Microwires Revealed by FastFourier-Transform Impedance Spectroscopy. J. Power Sources 2017, 349, 1−10.
(48) Loveridge, M. J.; Lain, M. J.; Johnson, I. D.; Roberts, A.; Beattie, S. D.; Dashwood, R.; Darr, J. A.; Bhagat, R. Towards High Capacity Li-Ion Batteries Based on Silicon-Graphene Composite Anodes and Sub-Micron V-Doped LiFePO 4 Cathodes. Sci. Rep. 2016, 6 (March), 1−11.
(49) Oumellal, Y.; Delpuech, N.; Mazouzi, D.; Dupre, N.; Gaubicher, J.; Moreau, P.; Soudan, P.; Lestriez, B.; Guyomard, D. The Failure Mechanism of Nano-Sized Si-Based Negative Electrodes for Lithium Ion Batteries. J. Mater. Chem. 2011, 21 (17), 6201−6208.
(50) (50) Kuziora, P.; Wyszynska, M.; Polanski, M.; Bystrzycki, J . Why the Ball to Powder Ratio (BPR) Is Insufficient for Describing the Mechanical Ball Milling Process. Int. J. Hydrogen Energy 2014, 39 (18), 9883−9887.
(51) Weckend, S.; Wade, A.; Heath, G. End-of-Life Management of Solar Photovoltaic Panels; International Renewable Energy Agency and International Energy Agency, 2016 (accessed May 15, 2018). Available from: https://www.Irena.org/Publications/2016/Jun/Endof-Life-Management-Solar-Photovoltaic-Pane.